The effect of the axial ligand on distinct reaction tunneling for methane hydroxylation by nonheme iron(IV)-oxo complexes

5 AUTHORS, INCLUDING:

Jia Guan
Texas A&M University
10 PUBLICATIONS **59** CITATIONS

SEE PROFILE

Xuri Huang
Jilin University
43 PUBLICATIONS **170** CITATIONS

SEE PROFILE

PCCP

PAPER

The effect of the axial ligand on distinct reaction tunneling for methane hydroxylation by nonheme iron(IV)–oxo complexes†

Hao Tang, Jia Guan, Lili Zhang, Huiling Liu* and Xuri Huang*

Comprehensive density functional theory computations on substrate hydroxylation by a range of nonheme iron(IV)–oxo model systems $[Fe^{IV}(O)(NH_3)_4L]^+$ (where L = $CF_3CO_2^-$, F^-, Cl^-, N_3^-, NCS^-, NC^-, OH^-) have been investigated to establish the effects of axial ligands with different degrees of electron donor ability on the reactivity of the distinct reaction channels. The results show that the electron-pushing capability of the axial ligand can exert a considerable influence on the different reaction channels. The σ-pathway reactivity decreases as the electron-donating ability of the axial ligand strengthens, while the π-pathway reactivity follows an opposite trend. Moreover, the apparently antielectrophilic trend observed for the energy gap between the triplet π- and quintet σ-channel (ΔG(T–Q)) stems from the fact that the reaction reactivity can be fine-controlled by the interplay between the exchange-stabilization benefiting from the ^5TS_H relative to the ^3TS_H by most nonheme enzymes and the destabilization effect of the σ_{z2}^* orbital by the anionic axial ligand. When the former counteracts the latter, the quintet σ-pathway will be more effective than the other alternatives. Nevertheless, when the dramatic destabilization effect of the σ_{z2}^* orbital by a strong binding axial σ-donor ligand like OH^- counteracts but does not override the exchange-stabilization, the barrier in the quintet σ-pathway will remain identical to the triplet π-pathway barrier. Indeed, the axial ligand does not change the intrinsic reaction mechanism in its respective pathway; however, it can affect the energy barriers of different reaction channels for C–H activation. As such, the tuning of the reactivity of the different reaction channels can be realised by increasing/decreasing the electron pushing ability.

1. Introduction

High-valent iron(IV)–oxo species which are invoked in a variety of the catalytic and enzymatic oxidation reactions that carry out essential oxidative transformations have attracted considerable interest.[1] In particular, the role of high-valent iron–oxo complexes in the activation of C–H bonds is of fundamental importance.[2,3] A well-known example is the active center in heme iron enzyme P450, which has been elaborated in depth.[4–6] Alternatively, many species that have also been characterized as the active center in heme iron enzymes such as peroxidases,[7–11] in nonheme enzymes such as α-ketoglutaratedioxygenase (TauD),[12–15] in iron containing zeolites[16,17] and in biomimetic complexes[18] are involved in C–H bond hydroxylation reactions. The fact is that a wide range of synthetic nonheme iron–oxo reagents are known to have low-spin triplet ground states,[19] except for

State Key Laboratory of Theoretical and Computational Chemistry, Institute of Theoretical Chemistry, Jilin University, Changchun, 130023, People's Republic of China. E-mail: huiling@jlu.edu.cn, huangxr@jlu.edu.cn; Fax: (+)86-43188498026; Tel: (+)86-13504404012
† Electronic supplementary information (ESI) available. See DOI: 10.1039/c2cp42423a

$[Fe^{IV}(O)(H_2O)_5]^{2+}$,[20] the $[Fe^{IV}(O)(TMG_3tren)]^{2+}$ ($TMG_3tren = N[CH_2CH_2N = C(NMe_2)_2]$) complex[21] and the recently reported synthetic high-spin iron(IV)–oxo species by Borovik.[22]

Indeed, a very large number of theoretical studies *via* mechanistic analysis in C–H bond activation have been reported by Solomon,[23] Thiel,[24] Shaik,[25,26] Siegbahn,[27] Baerends,[28,29] de Visser[30,31] and Neese *et al.*[32–34] Since Shaik and coworkers elaborated the important conception of two-state reactivity (TSR),[35] we can see that the quintet surface is seen to cut through the triplet barrier and to provide a low-energy path for C–H activation.[36,37] However, studies on how to rationalize the differential reactivity between quintet and triplet iron(IV)–oxo species have been extensively conducted. Shaik and coworkers proposed that the enhanced exchange interaction upon approaching the transition state (TS) on the quintet surface flattens the potential energy surface (PES) and hence lowers the barrier.[38] Furthermore, they have made contributions to the interplay between orbital- and exchange-controlled principles.[39,40] Baerends, Solomon, and coworkers showed that the degree of exchange stabilization in the high spin ferryl reactant is greater than the low spin analogues by stabilizing the Fe-σ_{z2}^* based σ-antibonding molecular orbital.[23,29,41–43] Additionally, the different optimal angles in the triplet and

This journal is © the Owner Societies 2012

Phys. Chem. Chem. Phys., 2012, **14**, 12863–12874 | 12863

quintet TSs, were pointed out by several authors.[31,34,36,38,41,44] More recently, all viable pathways in the same system for the alkane hydroxylation have been firstly proposed and they are significantly different in barrier height, with the order $^5\sigma > {}^5\pi > {}^3\pi > {}^3\sigma$.[32] In subsequent work, Neese and coworkers made contributions to the differential reactivity of the distinct spin states *via* an analysis of the electronic structure changes that occur upon alkane C–H bond hydroxylation by TauD[12–15] along the septet, quintet, and triplet reaction channels.[33] Thus, the factors that can affect the reactivity of different reaction channels are fascinating and constitute the focus for the present paper.

Moreover, one of the most intriguing discoveries is the remarkable importance of axial ligands in modulating the reactivity. Axial ligand effects have been studied extensively since Dawson *et al.* first proposed that the highly efficient O–O breaking ability of P450 can be attributed to the strong electron donation from the thiolate ligand in the proximal site of heme.[45–48] Experimentally, Gross *et al.*[49–51] and Nam *et al.*[37,52–58] have demonstrated the axial ligand effect on substrate oxidation by iron(IV)–oxo oxidants with variable axial ligands. Biomimetic iron–porphyrin oxidants were used in these studies, in which the ligand position *trans* to the oxo group was occupied by either an anion, *e.g.*, F⁻, Cl⁻, acetate, perchlorate, *etc.*, or a neutral solvent molecule, *e.g.*, acetonitrile. Thus, rate constants measured for styrene epoxidation and hydrogen abstraction reactions were found to vary with the nature of the axial ligand. Moreover, Nam and co-workers[53] demonstrated that the reaction of $[Fe^{IV}(O)(TPFPP^{+\bullet})X]$ with TPFPP = *meso*-tetrakis(pentafluorophenyl)porphyrinato and X = NCCH₃ or Cl⁻ and ethylbenzene could generate diverse products. They found that the reaction of $[Fe^{IV}(O)(TPFPP^{+\bullet})Cl]$ with ethylbenzene formed benzyl hydroxylation products, whereas that using $[Fe^{IV}(O)(TPFPP^{+\bullet})NCCH_3]^+$ as the oxidant led to aromatic hydroxylation instead. Furthermore, the computational studies on the axial ligand effect have been firstly conducted by de Visser and coworkers.[11] The theoretical

research of Kamachi *et al.*,[59] in which the activation effects on the cyclohexane hydroxylation reaction are revealed to rise from the anionic ligands coordinated to the iron(IV)–oxo porphyrin π-cation radical, confirmed the remarkable importance of axial ligands on modulating the reactivity. As for the precursor species $[Fe^{IV}(O)(H_2O)_5]^{2+}$, Bernasconi and Louwerse presented a detailed analysis of the effects of ligand substitution in simple gas-phase systems of composition $[Fe^{IV}(O)(H_2O)_n(L)_{5-n}]^{2+}$, with L = NH₃, CH₃CN, H₂S and BF₃.[41] Very recently, de Visser *et al.*[60] reported the effects of the axial ligand on spectroscopic parameters (*trans*-influence) as well as on aromatic hydroxylation kinetics (*trans*-effect) using a range of $[Fe^{IV}(O)(Por^{+\bullet})X]$ oxidants with X = SH⁻, Cl⁻, F⁻, OH⁻, acetonitrile, GlyGlyCys⁻, CH₃COO⁻, and CF₃COO⁻.

After the first report of a crystal structure of such a complex ($[Fe^{IV}(O)(TMC)(NCCH_3)]^{2+}$ (where TMC is 1,4,8,11-tetramethyl-1,4,8,11-tetraazacyclotetradecane)) by Rohde *et al.*[61] and the discovery of a number of additional nonheme iron(IV)–oxo complexes,[62–66] there has been much excitement in this field which led to extensive experimental and theoretical investigations employed to characterize the effect of the axial ligands on the activity of metal centers in these enzymes. For example, Rohde and Que proposed that the axial NCMe ligand in $[FeO(TMC)(L_{ax})]^{2+}$ leads to lower reactivity than the axial carboxylate ligand $CF_3CO_2^-$.[67] The similar nonheme complexes with anionic ligands, $[FeO(TMC)(NCS)]^+$ and $[FeO(TMC)(N_3)]^+$,[52] have been subsequently detected. More recently, experimental and theoretical endeavors to further validate the axial ligand effect on the ability of nonheme iron(IV)–oxo unit to carry out oxygen atom transfer to PPh₃ *versus* its ability to affect hydrogen atom abstraction of C–H and O–H bonds have been conducted by Shaik and coworkers.[37,54] Nam and coworkers examined the axial ligand influnce on the reaction of aliphatic and aromatic hydroxylation reactions by using $[Fe^{IV} = O(TMC)(L)]^{n+}$ (L = acetonitrile or chloride).[58] They found the system with the acetonitrile axial

$[Fe^{IV}(O)(NH_3)_4(O_2CCF_3)]^+$

r(Fe-O) = 1.63/1.62
r(Fe-N$_{eq}$) = 2.02/2.16
r(Fe-L$_{ax}$) = 2.07/2.03

$[Fe^{IV}(O)(NH_3)_4(F)]^+$

r(Fe-O) = 1.64/1.63
r(Fe-N$_{eq}$) = 2.02/2.16
r(Fe-L$_{ax}$) = 1.92/1.89

$[Fe^{IV}(O)(NH_3)_4(Cl)]^+$

r(Fe-O) = 1.63/1.63
r(Fe-N$_{eq}$) = 2.03/2.16
r(Fe-L$_{ax}$) = 2.45/2.38

$[Fe^{IV}(O)(NH_3)_4(NC)]^+$

r(Fe-O) = 1.63/1.63
r(Fe-N$_{eq}$) = 2.03/2.17
r(Fe-L$_{ax}$) = 2.04/2.02

$[Fe^{IV}(O)(NH_3)_4(N_3)]^+$

r(Fe-O) = 1.64/1.64
r(Fe-N$_{eq}$) = 2.03/2.17
r(Fe-L$_{ax}$) = 2.07/2.04

$[Fe^{IV}(O)(NH_3)_4(NCS)]^+$

r(Fe-O) = 1.63/1.63
r(Fe-N$_{eq}$) = 2.03/2.17
r(Fe-L$_{ax}$) = 2.04/2.00

$[Fe^{IV}(O)(NH_3)_4(OH)]^+$

r(Fe-O) = 1.65/1.65
r(Fe-N$_{eq}$) = 2.03/2.17
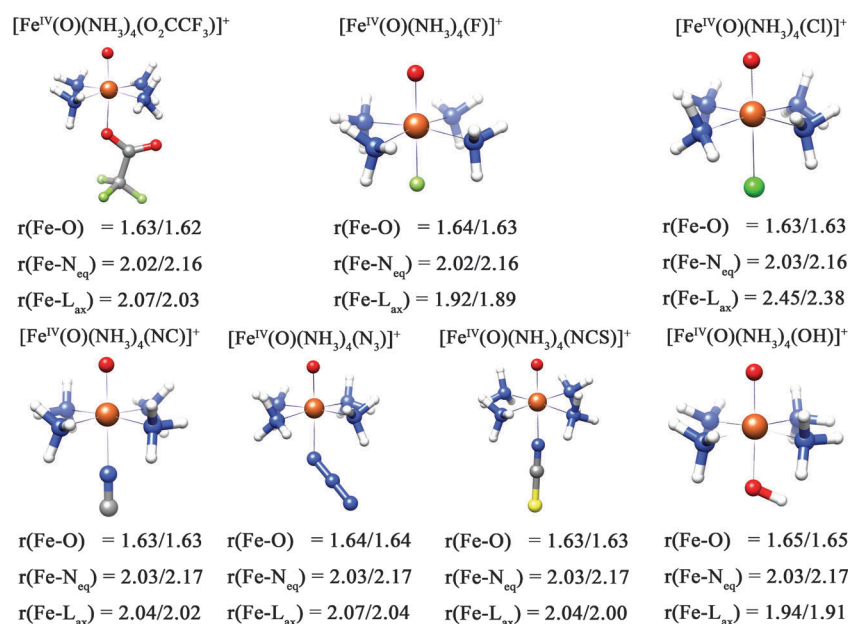r(Fe-L$_{ax}$) = 1.94/1.91

Fig. 1 Iron(IV)–oxo models studied in the reaction with methane. Bond lengths are in angstroms.

ligand is orders of magnitude more reactive than that with a chloride axial ligand. Moreover, the experimental and theoretical work has been mainly devoted to the spectroscopic properties and the donor properties.[55]

Inspired by these studies, we raise naturally some questions: (1) Whether there is a general trend of H-abstraction reactivity for the distinct reaction pathways in two-state C–H activation by a series of model systems? (2) If so, how would the reactivity trend of the distinct spin channel vary with the chosen set of axial ligands? (3) When increasing/decreasing the electron pushing ability of the axial ligands, how would the reactivity of the spin reaction channels be impacted?

By answering these questions, in this work we performed comprehensive first-principles DFT computations on substrate hydroxylation by a range of nonheme iron(IV)–oxo model systems with different axial anionic ligands, $[Fe^{IV}(O)(NH_3)_4(L)]^+$ (1-L) [where L is $CF_3CO_2^-$ (1-O$_2$CCF$_3$), F^- (1-F), Cl^- (1-Cl), NC^- (1-NC), N_3^- (1-N$_3$), NCS^- (1-NCS), OH^- (1-OH)] (Fig. 1), and specifically search for the effects of the axial ligands with different degrees of electron donor ability on the reactivity of the distinct reaction channels. To obtain all viable pathways in the same system for methane hydroxylation, precluding the steric hindrance effect of the equatorial ligands of the real complexes, we have chosen to model the ligand environment by using four equatorial NH_3 ligands and methane as substrate in all cases, although these systems are simplistic models of high-valent iron–oxo complexes rather than natural systems. In these models where the metal ion is surrounded by a distorted octahedral coordination environment of approximately C_{2v} symmetry, with four equatorial ligands in roughly planar geometry and one axial ligand in the axial position to the oxidant. The overall goal of this work is not to produce numbers that match some experimental values most closely but instead to obtain a general trend of H-abstraction reactivity for the reaction channels in two-state C–H activation by the chosen extensive model systems and elucidate the effect of the axial ligand on the distinct reaction channels, to formulate a coherent and predictive reactivity TSR model.
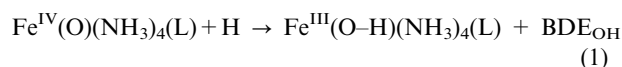
2. Computational methods

All calculations were performed with the ORCA program package.[68] The high molecular charge ($+1$) made it necessary to perform the optimization in solvent to avoid artificial results. The conductor like screen model (COSMO) was utilized for all calculations and acetonitrile was chosen as the solvent. We used the def2-TZVP basis sets[69] on the active atoms Fe, O, C and the transferred H atom as well as the hybrid B3LYP density functional[70,71] in combination with triple-ζ quality TZVP basis sets[72] on the remaining atoms. The RIJCOSX approximation[73] was used to accelerate the calculations in combination with the auxiliary basis sets def2-TZV/J (the active atoms Fe, O, C and the transferred H atom) and TZV/J (rest).[74–76] This kind of basis set system is labeled as B1. All of the geometries were fully optimized without symmetry constraints. Harmonic vibrational frequencies were computed to verify the nature of the stationary points. The minimum structures reported in this paper show only positive eigenvalues of the Hessian matrix, whereas the transition states (TSs) have only one negative eigenvalue. The zero-point

energies, thermal corrections and entropy terms for the optimized geometries were obtained from the frequency calculations.

Subsequent single point calculations were also performed with the hybrid B3LYP density functional using the new default basis sets of triple-ζ quality including high angular momentum polarization functions (def2-TZVPP)[77] for all elements. The density fitting and chain of spheres (RIJCOSX) approximations have been employed together with the def2-TZVPP/J auxiliary basis set,[78] labeled as B2.

Reorganization energies (RE_{FeOH}) were calculated as before from the difference in energy of the substrate in the transition state geometry and its fully relaxed structure.[26] The bond dissociation energy of the O–H bond in the iron(IV)-hydroxo complex with ligand L (BDE_{OH}) was calculated from eqn (1) with the same methods mentioned above, namely geometry optimizations using basis set B1, while energies are taken from single-point calculations with basis set B2.

$$Fe^{IV}(O)(NH_3)_4(L) + H \rightarrow Fe^{III}(O-H)(NH_3)_4(L) + BDE_{OH}$$
(1)

To ascertain that the methods are not influenced by the density functional method chosen here, we ran single point calculations using B3LYP with dispersion correction (B3LYP-D)[79] that was found to give more accurate binding energies.[80] In the present work, all calculations were performed with the ORCA program package, which includes the implementation of dispersion correction for energy and gradient and hence allows us to test the reaction barriers of TS$_S$ at the B3LYP-D level. Therefore, we use the B3LYP functional for geometry optimizations and upgrade the energies by single-point B3LYP-D calculation on B3LYP-optimized structures at the larger basis set (B2) level. As expected, B3LYP-D/B2//B3LYP/B1 gave generally similar trends as B3LYP/B2//B3LYP/B1.

Furthermore, we also used the PBE0 functional[81] to perform geometry optimizations in the H-abstraction step, since the PBE0 functional was tested successfully on spin-state ordering of $Fe(NH_3)_6^{2+}$ complexes.[82] Thus, we use the PBE0 functional for geometry optimizations at the B1 basis set level and upgrade the energies by single-point calculation on PBE0-optimized structures at the larger basis set (B2) level. All of the geometries were fully optimized without symmetry constraints. Harmonic vibrational frequencies were computed to verify the nature of the stationary points. The minimum structures show only positive eigenvalues of the Hessian matrix, whereas the transition states (TSs) have only one negative eigenvalue. The zero-point energies, thermal corrections and entropy terms for the optimized geometries were obtained from the frequency calculations. The B3LYP-D and PBE0 results predicted many of the reagents to have a quintet ground state, while the trends predicted by them are in general accord with the B3LYP results, and therefore we selected B3LYP as the choice method. The temperature and pressure for all the calculations were 298.15 K and 1.00 atm, respectively.

3. Results and discussion

3.1 Geometric features of the iron(IV)–oxo complexes

Fig. 1 shows the optimized geometries of the seven different iron(IV)–oxo oxidants and the critical bond lengths for all the

iron–oxo species in the triplet and quintet states. Focusing on the geometric details in Fig. 1 reveals Fe–O distances of 1.62–1.65 Å for all the complexes agree well with the crystallographically determined Fe=O bond distances in $[Fe^{IV}(O)TMC(X)]^{z+}$ reagents (with X = acetonitrile (MeCN), trifluoroacetate (TF), azide (N3), or thiolate (SR)), ranging from 1.64 to 1.68 Å.[61] The r(Fe–N) value, which was calculated by averaging four distances between the iron and equatorial nitrogen atoms, exhibits a fairly large spin-state dependence. Thus, in all cases, r(Fe–N) was the longest in the quintet state, in accordance with the occupation of the Fe-σ^*_{x2-y2} orbital, as previously found in P450 compound I[69] as well as in several nonheme iron–oxo species.[25,83] The calculated Fe–N distances of all the species are 2.02–2.03 Å in the triplet spin state, which match well the equatorial Fe–N distances in $[Fe^{IV}(O)TMC(X)]^{z+}$ reagents, 2.09 Å,[61] although the latter are slightly elongated due to the steric effects of the macrocyclic ligand. Furthermore, we found that the calculated structures of models 1-N₃ and 1-NCS more closely resembled those in the previously reported research on the systems $[FeO(TMC)(NCS)]^+$ and $[FeO(TMC)(N_3)]^+$,[37] that is, the azide ligand (N_3^-) coordinates to the iron center at an angle relative to the Fe=O axis, while the NCS^- ligand is collinear with this axis.

3.2 H-Abstraction reactions from CH₄ by iron(IV)–oxo oxidants

The C–H hydroxylation by the iron–oxo moiety is generally described as a H-abstraction/O-rebound mechanism, as proposed about 30 years ago by Groves and co-workers.[84] This mechanism is elaborated in two steps: one hydrogen atom is abstracted from the substrate RC by a TS ($^{2S+1}TS_H$), yielding an iron(III)-hydroxyl species together with a carbon radical (^{2S+1}I), namely the H-abstraction step. This intermediate collapses with the hydroxyl oxygen via a rebound TS ($^{2S+1}TS_{Re}$) to yield an iron(II) centre and the C–O bond of the alcohol complex (^{2S+1}P).

3.2.1 Orbital diagram analysis along the pathways. As shown previously, C–H bond cleavage is induced by a shift of an electron from the σ(C–H) bond orbital into the lowest acceptor molecular orbital of the FeO^{2+} species. Different from the lowest acceptor molecular orbital, the lowest unoccupied molecular orbital (LUMO) is directly related to the electrophilicity of the FeO^{2+} moiety. In a high spin configuration, the LUMO is the Fe-δ (β) orbital. The strong exchange field of the four unpaired α electrons significantly stabilizes the α orbitals.[25] Consequently, the Fe-σ^*_{z2}(α) orbital acts as an electron-accepting orbital for the quintet σ-pathway, whereas for the quintet π-mechanism it opens an alternative electron-transfer channel through the Fe-$\pi^*_{xz/yz}$(β) orbital. In the low spin configuration of π-mechanism where the exchange field stabilization is weaker,[33,39,40] and hence the Fe-$\pi^*_{xz/yz}$(β) orbital can be both the LUMO and the lowest acceptor orbital. However, the electron-accepting Fe-σ^*_{z2}(α) orbital of the triplet σ-pathway differs from the LUMO Fe-$\pi^*_{xz/yz}$(β) orbital.

C–H hydroxylations of methane by seven different iron(IV)–oxo oxidants are investigated. Electronically, these oxidants show many similarities, in particular, all oxidants have the same set of valence orbitals that determine their reactivity patterns.
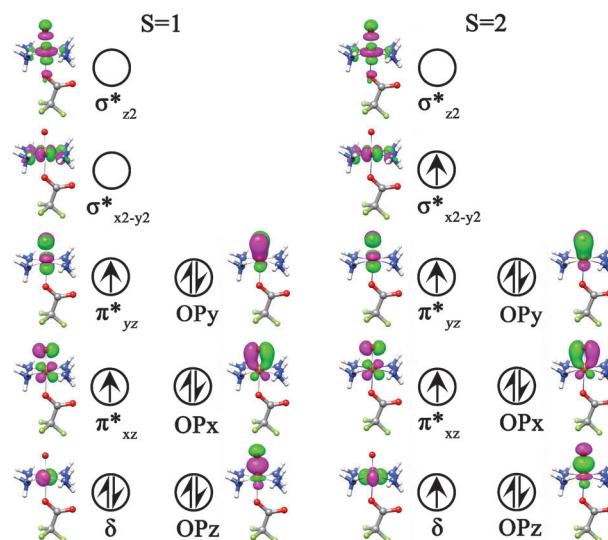

Fig. 2 Electron configurations corresponding to the triplet ($S = 1$) and quintet ($S = 2$) states of 1-O₂CCF₃.

For simplicity, let us mainly discuss on model system 1-O₂CCF₃ and collect the analogous results for the other models in the ESI.† The electron occupancies in the d-orbital of the triplet and quintet spin states of 1-O₂CCF₃ are depicted in Fig. 2. The δ orbital is nonbonding in the plane of the equatorial ligands, whereas the pair of $\pi^*_{xz/yz}$ orbitals is built up from the antibonding combination of the metal Fe-$d_{xz/yz}$ orbitals with the O-$p_{x/y}$ orbitals. The others are two σ* antibonding orbitals, one with the equatorial nitrogen atoms of NH₃(σ^*_{x2-y2}) and the other with the σ-orbitals on the oxo and axial ligand groups (σ^*_{z2}). The schematic molecular orbital diagrams for $^3TS_{H\sigma}$, $^3TS_{H\pi}$, $^5TS_{H\sigma}$, and $^5TS_{H\pi}$ for 1-O₂CCF₃ are shown in Fig. 3. It is herein, we primarily discuss the occupation pattern of the iron-centered d-orbital during the entire reaction.

$^5σ$-*Pathway.* For the quintet σ-pathway, the d^4 electrons in the reactant have a $(\delta)^1(\pi^*_{xz})^1(\pi^*_{yz})^1(\sigma^*_{x2-y2})^1(\sigma^*_{z2})^0$ occupation. As the electron of the substrate transferred into the Fe-σ^*_{z2} anti-bonding orbital, the corresponding $^5TS_{H\sigma}$ features a nearly collinear Fe–O–H arrangement with a $(\delta)^1(\pi^*_{xz})^1(\pi^*_{yz})^1(\sigma^*_{x2-y2})^1(\sigma^*_{z2})^1$ occupation. The radical intermediate $^5I_σ$ has the same orbital occupation $(\delta)^1(\pi^*_{xz})^1(\pi^*_{yz})^1(\sigma^*_{x2-y2})^1(\sigma^*_{z2})^1$ as $^5TS_{H\sigma}$. In the rebound step, the final electron acceptor is the weakly Fe-$\pi^*_{xz/yz}$ orbital for the 1-O₂CCF₃, 1-NCS, 1-NC and 1-Cl cases. Whereas for the 1-N₃, 1-F and 1-OH cases the rebound involves the second electron shift to δ orbital.

$^3π$-*Pathway.* The reactant in the triplet π-pathway has the configuration $(\delta)^2(\pi^*_{xz})^1(\pi^*_{yz})^1(\sigma^*_{x2-y2})^0(\sigma^*_{z2})^0$. The Fe-$\pi^*_{xz/yz}$ orbital accepts the electron from the substrate C–H bond, resulting in a change in orbital occupation by $(\delta)^2(\pi^*_{xz})^2(\pi^*_{yz})^1(\sigma^*_{x2-y2})^0(\sigma^*_{z2})^0$ and $(\delta)^2(\pi^*_{xz})^2(\pi^*_{yz})^1(\sigma^*_{x2-y2})^0(\sigma^*_{z2})^0$ for $^3TS_{H\pi}$ and $^3I_π$, respectively. Furthermore, in $^3TS_{Re\pi}$ and $^3P_π$, the configurations are $(\delta)^2(\pi^*_{xz})^2(\pi^*_{yz})^1(\sigma^*_{x2-y2})^0(\sigma^*_{z2})^0$, $(\delta)^2(\pi^*_{xz})^2(\pi^*_{yz})^1(\sigma^*_{x2-y2})^0(\sigma^*_{z2})^1$, respectively, reflecting that the second electron shift occurs from the orbital of the organic radical to the Fe-σ^*_{z2} orbital.
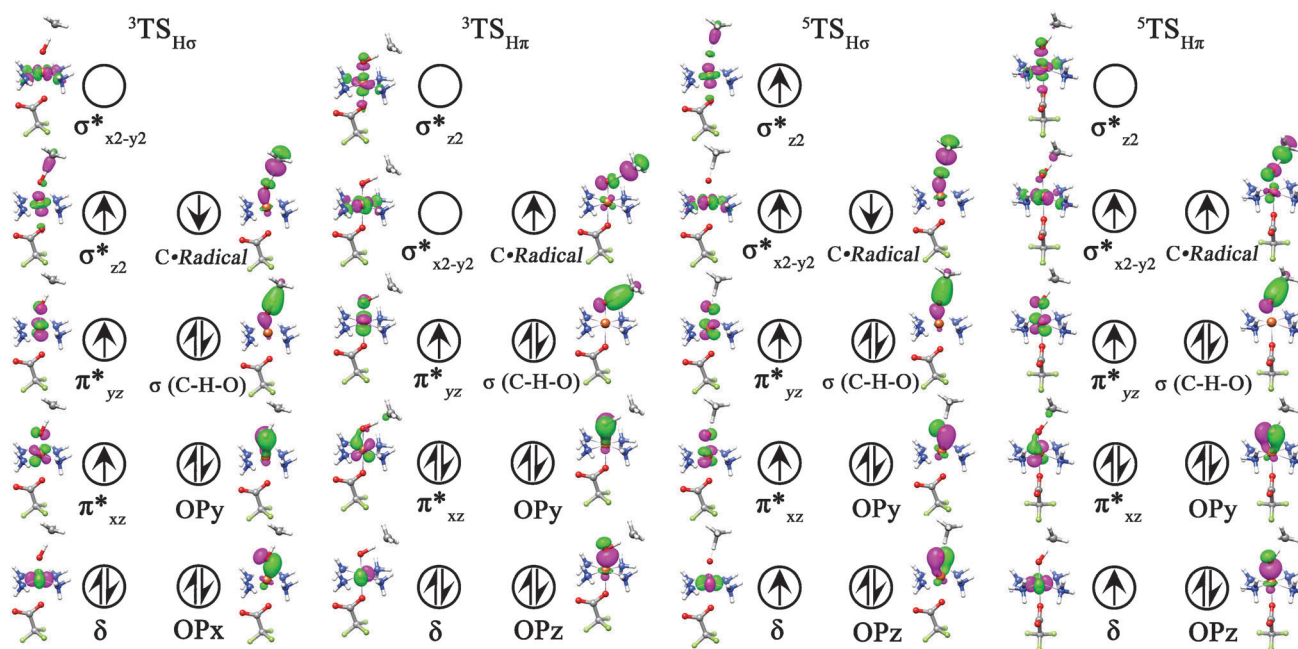
Fig. 3 Schematic MO diagram of $^3TS_{H\sigma}$, $^3TS_{H\pi}$, $^5TS_{H\sigma}$, and $^5TS_{H\pi}$ for $1\text{-}O_2CCF_3$.

$^5\pi$-*Pathway*. The schematic orbital diagram for $^5TS_{H\pi}$ shows that in the quintet π-pathway, this approach leads to the transfer of a β-rather than an α-spin electron into the Fe-$\pi^*_{xz/yz}$ orbital, similarly to what is commonly observed for the triplet π-pathway discussed above. For the $1\text{-}O_2CCF_3$, $1\text{-}N_3$, $1\text{-}NCS$, $1\text{-}NC$ and $1\text{-}Cl$ cases, the electron occupancies in the d-block orbitals along the oxidation pathway, possess a $(\delta)^1(\pi^*_{xz})^1(\pi^*_{yz})^1(\sigma^*_{x2-y2})^1(\sigma^*_{z2})^0$, $(\delta)^1(\pi^*_{xz})^2(\pi^*_{yz})^1(\sigma^*_{x2-y2})^1(\sigma^*_{z2})^0$, $(\delta)^1(\pi^*_{xz})^2(\pi^*_{yz})^1(\sigma^*_{x2-y2})^1(\sigma^*_{z2})^0$ configurations in $^5RC_\pi$, $^5TS_\pi$, and $^5I_\pi$, respectively. Starting from $^5I_\pi$, the rebound step follows a σ-mechanism, in which the remaining α-electron of the methyl radical is transferred to the Fe-σ^*_{z2} orbital and leads to forming a Fe(II) ion.

In contrast to the 1-F and 1-OH cases in which the $^5RC_\pi$ and $^5TS_\pi$ have the same electronic structures as those in the $1\text{-}O_2CCF_3$, $1\text{-}N_3$, $1\text{-}NCS$, $1\text{-}NC$ and $1\text{-}Cl$ cases, a different electronic structure of the $^5I_\pi$ is obtained. Interestingly, the $(\delta)^2(\pi^*_{xz})^1(\pi^*_{yz})^1(\sigma^*_{x2-y2})^1(\sigma^*_{z2})^0$ electron configuration calculated in $^5I_\pi$ of the 1-F and 1-OH cases does not reach the idealized orbital occupation of $(\delta)^1(\pi^*_{xz})^2(\pi^*_{yz})^1(\sigma^*_{x2-y2})^1(\sigma^*_{z2})^0$ for quintet π-mechanism. The axial ligand F^-/OH^- has much stronger π antibonding interaction with the Fe-$\pi^*_{xz/yz}$ orbital and hence induces the electron redistribution from the Fe-$\pi^*_{xz/yz}$ orbital to δ orbital during the transformation of $^5TS_{H\pi}$ to $^5I_\pi$. Based on the unusual electron configuration of $^5I_\pi$, the $^5TS_{Re\pi}$ shares the same stable configuration with $^5I_\pi$, while the $^5P_\pi$ has a $(\delta)^2(\pi^*_{xz})^1(\pi^*_{yz})^1(\sigma^*_{x2-y2})^1(\sigma^*_{z2})^1$ configuration, both of which are attended by an electron shift from the orbital of the organic radical to the Fe-σ^*_{z2} orbital. This is in good agreement with the previous studies on the quintet π-mechanism for alkane hydroxylation by iron(IV)–oxo complexes.[32] Additionally, close inspection of the reactivity indicates that the quintet π-channel may encounter a comparable barrier to that calculated

on the triplet surface due to the unavoidably increased Pauli repulsion and the reduced orbital overlap relative to the quintet σ-pathway.

$^3\sigma$-*Pathway*. The triplet σ-mechanism encounters much higher energy barrier than that for the corresponding process on the quintet surface, due to the substantially reduced exchange stabilization generated by three rather than five unpaired electrons in the low spin ferric center.[33] Moreover, the molecular orbital diagrams for $^3\sigma TS_H$ of $1\text{-}O_2CCF_3$ in Fig. 3 also show that, the d^4 electrons have a $(\delta)^2(\pi^*_{xz})^1(\pi^*_{yz})^1(\sigma^*_{x2-y2})^0(\sigma^*_{z2})^0$ electron configuration in the reactant. As H-abstraction occurs, an α-spin electron transfers into the lowest acceptor Fe-σ^*_{z2} antibonding orbital, and generates $^3TS_{H\sigma}$ with a $(\delta)^2(\pi^*_{xz})^1(\pi^*_{yz})^1(\sigma^*_{x2-y2})^0(\sigma^*_{z2})^1$ configuration. The intermediate $^3I_\sigma$ is characterized by a $(\delta)^2(\pi^*_{xz})^1(\pi^*_{yz})^1(\sigma^*_{x2-y2})^0(\sigma^*_{z2})^1$ configuration. Like the π-pathway, the electron-transfer pathway for the hydroxylation product starts with $^3I_\sigma$ and then the radical shifts its β electron to the Fe-$\pi^*_{xz/yz}$ orbital while making the C–O bond of the alcohol complex. Clearly, the electronic transfer pattern for the triplet σ-mechanism of 1-Cl case closely resembles that found in the $1\text{-}O_2CCF_3$ case.

For 1-NC and 1-NCS, the electronic transfer pathways of the first H-abstraction are the same as those found in the $1\text{-}O_2CCF_3$ and 1-Cl cases, that is, an α electron shift into the Fe-σ^*_{z2} orbital. Unlike the $1\text{-}O_2CCF_3$ and 1-Cl cases, the $^3I_\sigma$ intermediate of 1-NC or 1-NCS is anomalous in its geometric and electronic structure. Notably, the Fe–O–H rearrangement has significantly changed from a collinear geometry to a bent unit, yielding the very stable electronic configuration $(\delta)^2(\pi^*_{xz})^1(\pi^*_{yz})^1(\sigma^*_{x2-y2})^1(\sigma^*_{z2})^0$ in $^3I_\sigma$ when going from $^3TS_{H\sigma}$ to intermediate $^3I_\sigma$. This may rationalize the observation that, compared with the other channels ($^5\sigma$, $^3\pi$, $^5\pi$), $CF_3CO_2^-$ and Cl^-

in the triplet σ-mechanism have a much stronger σ antibonding interaction with the Fe-σ^*_{z2} orbital. During the transformation of $^3TS_{H\sigma}$ to intermediate $^3I_\sigma$, the orbital modulation finally results in electron transfer to the Fe-σ^*_{x2-y2} orbital. Therefore, the $^3TS_{Re\sigma}$ exhibits the same electronic configuration as that of $^3I_\sigma$. In the rebound step, as observed, the electron of the radical going to fill the Fe-$\pi^*_{xz/yz}$ orbital creates the $^3P_\sigma$ with a $(\delta)^2(\pi^*_{xz})^2(\pi^*_{yz})^1(\sigma^*_{x2-y2})^0(\sigma^*_{z2})^1$ configuration.

3.2.2 General reactivity patterns in the data set. Our foregoing discussion focused on the electronic character of different reaction tunnelings by orbital diagram analysis. To facilitate this discussion, we have collected the data in the Tables and Figures as follows: Fig. 4 shows the detailed geometric features of the transition states for C–H cleavage. The corresponding rebound $^{2S+1}TS_{Re}$ structures are displayed in Fig. 5. The data for the spin population variation along the σ- and π-reaction pathways in two spin states for 1-O$_2$CCF$_3$ are collected in Table 1 (the others see Table S3 in the ESI†), while Mulliken charge analysis of all the species are displayed in Table S4 in the

ESI.† All the data for the barriers of H-abstraction and the corresponding rebound barriers are shown in Table S1 and S2 in the ESI.†

Geometric features of the transition states. Optimized geometries of the triplet and quintet transition states of all the substrates are illustrated in Fig. 4. As the substrate approaches the iron(IV)–oxo unit, the Fe–O distance gradually elongates. For the π-pathway, when the strong Fe–O π antibonding $\pi^*_{xz/yz}$ orbital accepts an electron, it eliminates one of the $2 \times 1/2$ Fe–O π-bonds. The weakening of the Fe–O π-bond by this additional electron leads to a distortion (*i.e.*, elongation) of the Fe–O bond length in the transition state. The $\Delta r(Fe–O)$ $(\Delta r(Fe–O) = r_{ts}(Fe–O) - r_r(Fe–O))$ in $^3TS_{H\pi}$ and $^5TS_{H\pi}$ have similar distances (0.13 Å–0.16 Å), which are slightly longer than those in $^5TS_{H\sigma}$ (0.12 Å–0.16 Å). The phenomenon obtained is attributed to the occupation of the Fe-σ^*_{z2} orbital by an electron. The Fe–O distances in the triplet σ-pathway, which can be clearly observed only in 1-O$_2$CCF$_3$, 1-NC, 1-Cl, 1-F, 1-NCS complexes, elongate greatly (by 0.15 Å–0.17 Å).
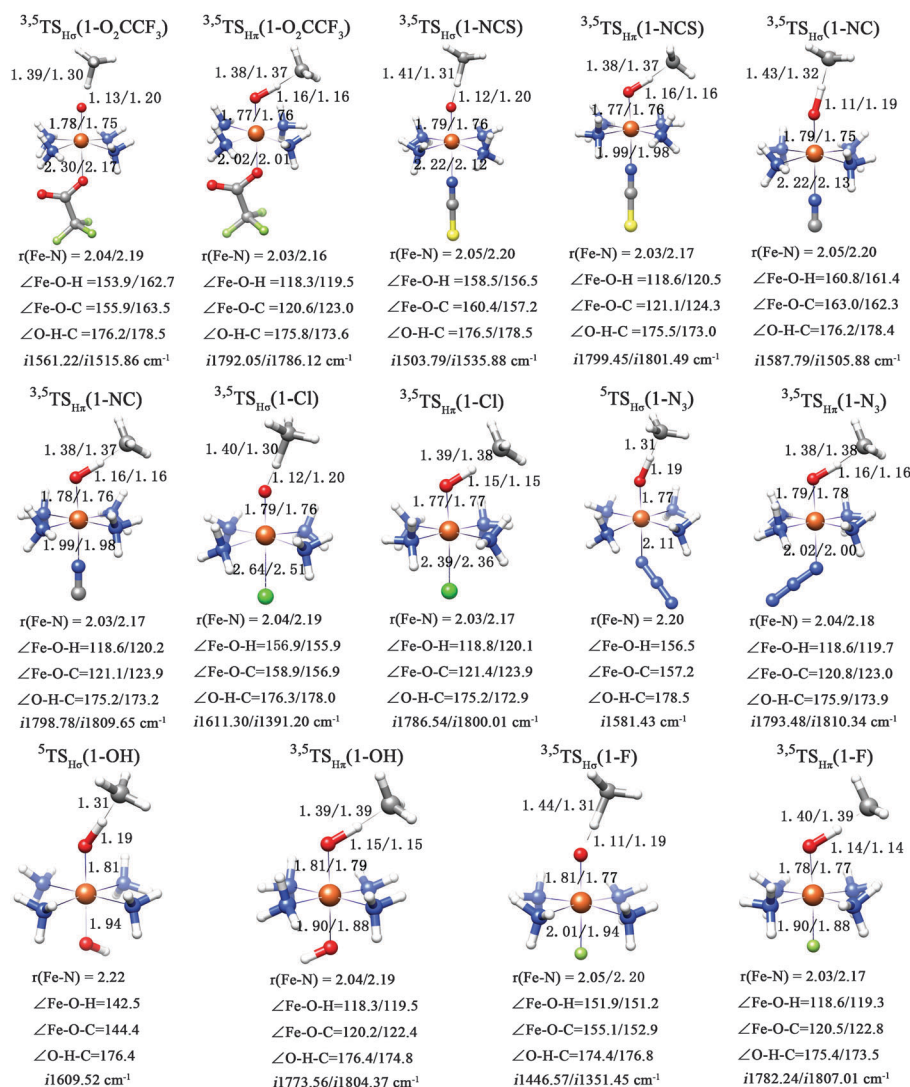

Fig. 4 Geometric details of hydrogen-abstraction transition states for the triplet/quintet spin states. Bond lengths are in angstroms and angles are in degrees.

In addition, the Fe–N_{eq} distance is obviously longer in the quintet than that in the triplet spin state, in accordance with the occupation of the Fe-σ^*_{x2-y2} orbital. The $\Delta r(Fe–N_{eq})$ ($\Delta r(Fe–N_{eq}) = r_{ts}(Fe–N_{eq}) - r_r(Fe–N_{eq})$) of all the complexes is found in a small range of 0.01 Å–0.05 Å and ~0.02 Å for $^{3,5}TS_{H\sigma}$ and $^{3,5}TS_{H\pi}$, respectively. Here the distance for the σ-mechanism is slightly elongated with respect to the π-mechanism owing to the occupation of the Fe-σ^*_{z2} orbital. Another salient characteristic that occurs upon approaching the transition state is the Fe–O–H angle in TS_H. Fig. 4 depicts the optimized geometries of $^{3,5}TS_H$ in the reaction by the $[Fe^{IV}(O)(NH_3)_4L]^+$ complexes with CH_4. Accordingly, the Fe–O–H angles are about 120° (the deviation from 90° reflects the compromise between the orbital interactions and Pauli repulsion)[33] in the transition state for the π-pathway, because the Fe-$\pi^*_{xz/yz}$ orbital serves as an electron acceptor and hence the substrate approaches the oxidant sideways. By contrast, these angles for the σ-pathway are close to 170°, since on this surface the shift occurs on the Fe-σ^*_{z2} orbital that lies on the Fe–O axis. Indeed, an Fe–O–H angle of 118.3°–118.8° and a value of 119.3°–120.5° were observed in the triplet and quintet π-pathways, respectively, while the Fe–O–H angles in the triplet and quintet σ-pathways were found to be 151.9°–160.8° and 142.5°–162.7°, supporting the bent and upright orientations of these TSs in the π- and σ-pathways.

Geometric features of the rebound transition states. Further support for the orbital diagram comes from the rebound transition states in Fig. 5. It is seen that the trends in the Fe–O–C angles of the $^{3,5}TS_{Re}$ are opposite to those discussed for $^{3,5}TS_H$. Thus, the corresponding rebound transition state in the π-pathway follows a σ-mechanism with the Fe–O–C angles of 154.8°–158.4° ($^3TS_{Re}$) and 160.5°–170.4° ($^5TS_{Re}$), indicating that the second electron transfers from the orbital of the organic radical to the vacant Fe-σ^*_{z2} orbital to maximize the overlap between the C• radical and Fe-σ^*_{z2} orbital. By contrast, the TS_{Re} in the σ-pathway is accompanied by electron transfer from the substrate to the δ orbital, and the Fe–O–C angle is accordingly smaller.

Spin population analysis. The key character of the mechanism can be understood by inspecting the spin population development along the reaction paths. Table 1 assembles all the data of the spin population of 1-O_2CCF_3. On the σ-mechanism surface, as H-abstraction occurs, the electron that shifts initially from σ(C–H) is a spin-up electron, hence the spin density in the triplet and quintet state reveals that the organic molecule (CH_3) develops a radical character that reaches −0.97 and −0.96 at the intermediate stage, while the spin on the H^b (transferred hydrogen) climbs, reaching 0.05 and 0.02 at the transition stage. At the same time, the electron shifts into the Fe-σ^*_{z2} orbital of iron(IV)–oxo, thus the spin on the oxo atom attenuates from 0.77 to 0.01 in $^3\sigma$, from 0.60 to 0.01 in

$^{3,5}TS_{Re\sigma}(1-O_2CCF_3)$
2.31/2.43
0.96/0.96
1.92/1.88
2.36/2.19
r(Fe–N) = 2.05/2.20
∠Fe-O-C = 133.4/130.4
$i422.87/i286.09$ cm^{-1}

$^{3,5}TS_{Re\pi}(1-O_2CCF_3)$
2.19/2.53
0.97/0.97
1.90/1.84
2.10/2.04
r(Fe–N) = 2.04/2.18
∠Fe-O-C =157.5/168.5
$i560.76/i244.04$ cm^{-1}

$^{3,5}TS_{Re\sigma}(1-NCS)$
2.17/2.53
0.97/0.96
1.91/1.85
2.06/2.01
r(Fe–N) = 2.19/2.22
∠Fe-O-C =131.4/130.8
$i496.44/i289.70$ cm^{-1}

$^{3,5}TS_{Re\pi}(1-NCS)$
2.26/2.43
0.97/0.97
1.84/1.89
1.99/2.12
r(Fe–N) = 2.05/2.19
∠Fe-O-C =158.1/161.1
$i591.93/i252.57$ cm^{-1}

$^{3,5}TS_{Re\sigma}(1-NC)$
2.26/2.44
0.96/0.97
1.84/1.88
2.00/2.14
r(Fe–N) = 2.19/2.22
∠Fe-O-C =131.2/128.7
$i497.60/i285.75$ cm^{-1}

$^{3,5}TS_{Re\pi}(1-NC)$
2.32/2.43
0.96/0.96
1.91/1.89
2.85/2.52
r(Fe–N) = 2.05/2.19
∠Fe-O-C =157.6/170.4
$i615.28/i304.02$ cm^{-1}

$^{3,5}TS_{Re\sigma}(1-Cl)$
2.15/2.46
0.97/0.97
1.92/1.86
2.06/2.0l
r(Fe–N) = 2.05/2.21
∠Fe-O-C =133.5/130.6
$i413.67/i292.44$ cm^{-1}

$^{3,5}TS_{Re\pi}(1-Cl)$
2.21/2.55
0.97/0.97
1.90/1.85
2.46/2.39
r(Fe–N) = 2.04/2.18
∠Fe-O-C =158.4/165.8
$i538.27/i228.10$ cm^{-1}

$^5TS_{Re\sigma}(1-N_3)$
2.39
0.96
1.90
2.11
r(Fe–N) = 2.22
∠Fe-O-C =131.6
$i324.63$ cm^{-1}

$^{3,5}TS_{Re\pi}(1-N_3)$
2.16/2.49
0.97/0.97
1.93/1.86
2.09/2.03
r(Fe–N) = 2.05/2.19
∠Fe-O-C =156.4/163.5
$i595.91/i269.32$ cm^{-1}

$^5TS_{Re\sigma}(1-OH)$
2.27
0.96
1.94
1.95
r(Fe–N) = 2.25
∠Fe-O-C =131.7
$i414.29$ cm^{-1}

$^{3,5}TS_{Re\pi}(1-OH)$
2.03/2.34
0.97/0.97
1.98/1.87
1.97/1.88
r(Fe–N) = 2.05/2.23
∠Fe-O-C =154.8/160.5
$i714.11/i424.33$ cm^{-1}

$^{3,5}TS_{Re\sigma}(1-F)$
2.16/2.30
0.97/0.96
1.85/1.91
1.87/1.96
r(Fe–N) = 2.20/2.23
∠Fe-O-C =130.6/130.3
$i607.57/i379.04$ cm^{-1}

$^{3,5}TS_{Re\pi}(1-F)$
2.10/2.42
0.97/0.97
1.93/1.84
1.97/1.85
r(Fe–N) = 2.04/2.22
∠Fe-O-C =155.4/165.8
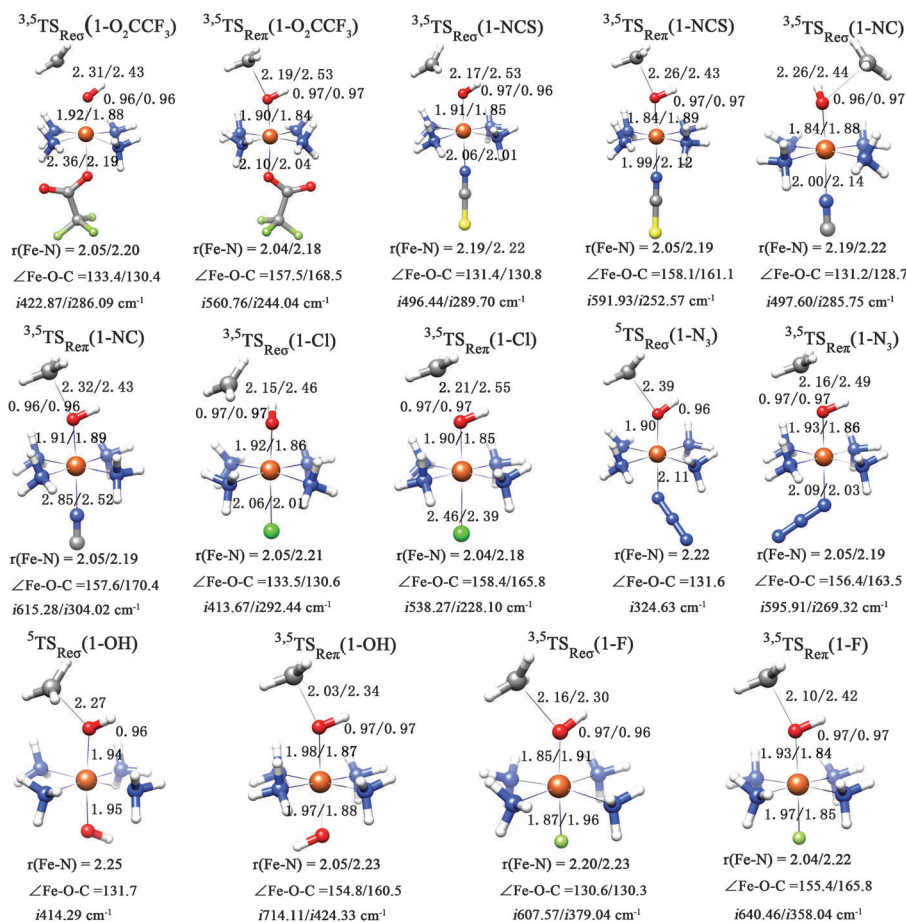$i640.46/i358.04$ cm^{-1}

Fig. 5 Geometric details of the rebound transition states in this study. Wherever available, each datum is given two numbers corresponding to triplet/quintet, respectively.

Table 1 Spin population of the reactant, transition state, intermediate, and product for $[Fe^{IV}(O)(NH_3)_4(CF_3CO_2)]^{+ \, a}$

		Fe	O	CH_3	H^b
RC	$3\sigma/3_\Pi$	1.29/1.29	0.77/0.77	0.00/0.00	0.00/0.00
	$5\sigma/5_\Pi$	3.15/3.15	0.60/0.60	0.00/0.00	0.00/0.00
TS_H	$3\sigma/3_\Pi$	2.55/0.99	0.14/0.53	−0.67/0.59	0.05/−0.05
	$5\sigma/5_\Pi$	3.98/2.91	0.11/0.43	−0.46/0.56	0.02/−0.04
I	$3\sigma/3_\Pi$	2.76/0.99	0.27/0.10	−0.97/0.97	0.01/0.00
	$5\sigma/5_\Pi$	4.19/2.86	0.35/0.05	−0.96/0.97	0.01/0.00
TS_{Re}	$3\sigma/3_\Pi$	2.61/1.32	0.26/−0.07	−0.82/0.82	0.01/0.01
	$5\sigma/5_\Pi$	4.10/3.26	0.30/−0.17	−0.72/0.77	0.01/0.01
P	$3\sigma/3_\Pi$	2.04/2.03	0.01/0.01	0.01/0.01	0.00/0.00
	$5\sigma/5_\Pi$	3.81/3.82	0.01/0.01	0.01/0.01	0.00/0.00

[a] Values from Mulliken population analysis. [b] The transferred hydrogen.

$^5\sigma$, while the spin on the iron ion in $^3\sigma$ climbs from 1.29 to 2.04 and from 3.15 to 3.81 in the $^5\sigma$. In $^5P_\sigma$ and $^3P_\sigma$, there is significant d-orbital delocalization toward the oxygen ligand. As a result, the spin values of 3.81 and 2.04 for $^5\sigma$ and $^3\sigma$ are much smaller than the ideal values, namely, 4 for $^5P_\sigma$ that has four singly occupied d-type orbitals and 2 for $^3P_\sigma$ formed by two singly occupied d-type orbitals. For the π-mechanism, a spin-down electron transfers from the σ(C–H) orbital of the substrate to the Fe-$\pi^*_{xz/yz}$ orbital of the iron(IV)–oxo reagent. There are similarities and differences with the σ-mechanism. Due to the formation of the O–H bond, the spin on the oxo atom is depleted from 0.77 to 0.01 in $^3\pi$, from 0.60 to 0.01 in $^5\pi$, which is similar to the σ-mechanism. The first difference is the spin density on the organic molecule (CH_3) possessing a singly occupied orbital that peaks at the intermediate stage and then vanishes as the R–OH bond is formed. The second is the jump in the iron spin population from 3.15 to 3.82 in $^5\pi$, from 1.29 to 2.03 in $^3\pi$. The third is that the spin on the iron H^b diminishes, reaching −0.05 and −0.04 at the transition stage in $^3\pi$ and $^5\pi$. In the end, the $C^\bullet$ radical orbital combines with the oxygen orbital of the remaining σ(FeO), and they evolve together to produce the σ(CO) orbital of the final product alcohol.

3.3 Energy profiles for C–H hydroxylation reaction between $[Fe^{IV}(O)(NH_3)_4L]^+$ and CH_4

In summary, the reactions proceed *via* both σ- and π-pathways in the triplet and quintet spin states, namely $^3\sigma$, $^3\pi$, $^5\sigma$ and $^5\pi$. A typical example of the reaction profile of C–H bond hydroxylation by 1-O_2CCF_3 is illustrated in Fig. 6. On the triplet surface, the free energy barrier for σ/π-pathway was found to be 34.60 and 24.57 kcal mol^{-1} relative to the separate reactants, while the energy barriers in the quintet spin state for the σ-/π-pathway were 24.57/29.17 kcal mol^{-1}, respectively. However, as shown recently by Lonsdale *et al.*[85] and found herein too, inclusion of dispersion correction lowers the H-abstraction barriers by 4–6 kcal mol^{-1} to 16.33/20.94 kcal mol^{-1} for $^5\sigma/^3\pi$ and 23.52/30.19 kcal mol^{-1} for $^5\pi/^3\sigma$, respectively.

For the 1-F, 1-Cl, 1-NCS, 1-NC cases, the corresponding energy profiles have similar characteristics and are collected in the ESI (see Fig. S2a–S2d).† The dispersion correction also decreases the reaction barriers of the cases, which highlights the very significant effect of van der Waals interaction.[79,80,85,86] Fig. S2e† displays the energy profile for hydroxylation of CH_4 by 1-N_3 model. The B3LYP energetic barriers for the reaction were 20.01, 22.97 and 24.84 kcal mol^{-1} for $^5\sigma$,
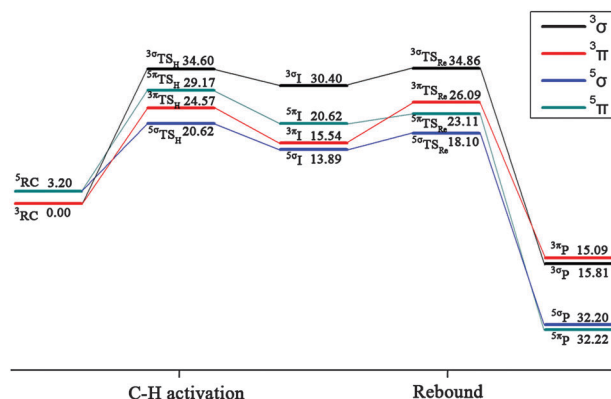

Fig. 6 The energy profile of methane hydroxylation by the 1-O_2CCF_3 in all the pathways on the triplet and quintet surfaces at the B3LYP/B2//B3LYP/B1 level.

$^3\pi$ and $^5\pi$, respectively. B3LYP-D lowers these barriers by 2–3 kcal mol^{-1} to 17.98, 21.59 and 21.33 kcal mol^{-1} for $^5\sigma$, $^3\pi$ and $^5\pi$, respectively.

Much like the 1-N_3 case, the reaction by 1-OH, in Fig. S2f,† also involves possible $^5\sigma$, $^3\pi$, $^5\pi$ channels. The corresponding barriers were 21.00, 23.21 and 25.00 kcal mol^{-1}, respectively. After adding dispersion correction, the barriers decrease to 18.63, 21.84 and 21.64 kcal mol^{-1}, respectively.

Through comparing the calculated energy barriers for hydrogen-atom abstraction in all viable pathways, we can see that the relative reactivity of all the $[Fe^{IV}(O)(NH_3)_4L]^+$ reagents decreases in the order $^5\sigma > ^3\pi > ^5\pi > ^3\sigma$, with both the B1 and B2 basis sets. While considering the dispersion correction, the similar reactivity trend: $^5\sigma > ^3\pi \approx ^5\pi > ^3\sigma$ was observed. This conclusion is consistent with a previous study.[32,87]

Turning now to the barrier gap between the $^3\pi$ and $^5\sigma$ (ΔG(T-Q)), we can see a general trend, namely from L = F$^-$, NCS$^-$, Cl$^-$, CF$_3$CO$_2^-$, N$_3^-$, NC$^-$ to OH$^-$, the $^5\sigma$ progressively approaches the $^3\pi$, with the corresponding ΔG(T-Q) gap of 5.40, 4.60, 4.30, 4.00, 3.00, 2.40, 2.21 kcal mol^{-1} at the B3LYP/B2//B3LYP/B1 level.

As far as the rebound step is concerned, the triplet rebound step involves a rather high barrier in contrast to the corresponding one on the quintet surface. The feature is clearly apparent in the triplet π-channel and the quintet σ-pathway. The reason for that is the weakly π-antibonding orbital and strongly σ-antibonding orbital serve as the final electron acceptor for quintet σ- and triplet π-mechanism, respectively.

From the above discussion, our most theoretical results can follow reasonable general trends for H-atom abstraction, such that the quintet σ-pathway has by far the lowest barrier among the other alternatives in these cases.

4. Discussion

4.1 The trends in the spin-state ordering of $^3[Fe^{IV}(O)(NH_3)_4L]^+$ complexes

Inspection of the energy profiles for C–H activation by $[Fe^{IV}(O)(NH_3)_4L]^+$ toward CH_4 revealed that the model systems have a triplet ground state ($S = 1$), and a low-lying excited-quintet state ($S = 2$) with $(\delta)^1(\pi^*_{xz})^1(\pi^*_{yz})^1(\sigma^*_{x^2-y^2})^1(\sigma^*_{z^2})^0$ occupancy.

The B3LYP calculations show that the Gibbs free energies in the triplet and quintet states lie close and the quintet surface cuts through the triplet barrier, thereby providing in principle a low-energy path for the reactions. In terms of the fact that the two spin-state surfaces are so close and cross throughout the H-abstraction channel the probability of such a crossover seems significant. We shall therefore consider TSR and discuss the likelihood of the spin inversion from the triplet ground state to an excited quintet spin state for these $[Fe^{IV}(O)(NH_3)_4L]^+$ model complexes.

As seen previously,[36,40] the spin-state ordering depended on the interplay of the δ-σ^*_{x2-y2} orbital energy gap and the exchange interactions among the unpaired electrons in the d-block. The δ-σ^*_{x2-y2} orbital energy gap mainly consists of two factors: (i) the binding strength of the equatorial Fe–N bonds, (ii) the electron–electron repulsion between the electrons of axial ligand and the electron pair in the δ orbital in the triplet state. Among the oxidants studied in this paper, the σ interactions between the σ^*_{x2-y2} orbital and the equatorial NH_3 ligands lead to the significant gaps between δ and σ^*_{x2-y2} orbitals and therefore the ground state has a triplet spin state, $S = 1$, with two unpaired electrons. Furthermore, if the repulsion between the electron of the axial ligand and the electron pair in the δ orbital of Fe is strong, the electron transfer from the δ orbital to the σ^*_{x2-y2} orbital would easily occur and then stabilize the quintet state. The series with different axial ligands show apparent signs for the electron–electron repulsion with the axial ligand. For example, the 1-O_2CCF_3 and 1-F cases with weaker electron pushing ability have a larger gap, while the 1-OH case, where the axial ligand possesses a stronger σ-donor, has the smaller gap. It is seen that the orbital energy gap prefers the triplet state, whereas the exchange energy favors the quintet state. As such, the compromise between the orbital energy gap and the exchange energy yields a much closer energy of the triplet and quintet states as found in the $[Fe^{IV}(O)(NH_3)_4L]^+$ model systems. This fine balance may provide a probability that a fast pre-equilibrium between the triplet and quintet reactants could exist, and then be followed by a reaction from the quintet state alone. This is in good agreement with one of the mechanistic TSR scenarios described by Shaik;[36] that when the energy gap between the triplet and quintet states is very small, there is a spin-state pre-equilibrium followed by activation on the quintet surface.

## 4.2 Axial ligand influence on the reaction channels

After finishing the analysis of the likelihood of the two spin-state ordering inversion, we now turn to elucidation of the axial ligands' influence on the reaction channels. As we mentioned above, all the C–H activation reactions by the $[Fe^{IV}(O)(NH_3)_4L]^+$ model systems with CH_4 involve two-state reactivity (TSR), whereby the quintet state starts as an excited state, albeit of low energy, but in the TS_H region the π-channel on the triplet (T) surface eventually crosses over to the quintet (Q) σ-surface. This computed result is in accordance with previous studies which showed that the quintet σ-pathway is more reactive toward C–H bond activation than the triplet π-channel.[36,37] As argued before,[33] this result may be ascribed

to the synergy of the geometric rearrangement, the Pauli repulsion between the substrate and the iron–oxo species, the orbital interaction between the electron donor and acceptor orbitals, and the spin polarization effect. The H-atom abstraction for the σ-pathway requires an essentially linear attack, which can significantly reduce the Pauli repulsion between the substrate and the iron(IV)–oxo reactant in comparison with the π-pathway. By contrast, a π-channel is operative on the triplet surface that results in an optimal attack angle near 90°. However, the latter is not possible due to a larger Pauli repulsion. The spin-polarization stabilization created by five unpaired electrons in the high spin Fe center in ^5TS_H is much stronger relative to only one unpaired electron in the low spin iron(III) in the corresponding ^3TS_H.[33,39,40] Additionally, the structural deformation energies may affect the H-abstraction barriers.[87] Taken together, the above analysis implies that the cooperation of the minimal Pauli repulsion, the favorable orbital interactions, the strong exchange stabilization and the proper structural deformation energies render the quintet σ-pathway more effective for H-atom abstraction reactions than the triplet π-pathway.

Besides the above contributions, we also explored the effect of the axial ligands decorated by different acceptor/donor groups on the differential reactivity of the reaction channels. Scheme 1 displayed the general trend of H abstraction reactivity by the electron pushing ability of different axial ligands. The behavior of the $[Fe^{IV}(O)(NH_3)_4L]^+$ complexes in H-atom abstraction reactions for the σ- and π-pathways exhibits a inverted reactivity pattern. Interestingly, whereas the σ-pathway reactivity follows the general trend of the antielectrophilicity of the oxidant, the π-pathway reactivity follows an opposite trend.

Considering the π-pathway surfaces, calculated results show that the reactivity ordering for the triplet vs. the quintet is: $L = N_3^- > OH^- > NC^- > NCS^- > CF_3CO_2^- > Cl^- > F^-$ vs. $L = N_3^- > OH^- > NC^- > NCS^- > Cl^- > CF_3CO_2^- > F^-$, respectively. It is apparent that in the π-pathway the more electron-donating the axial ligand is, the more reactive the iron(IV)–oxo species becomes in H-atom abstraction.

In parallel, on the quintet and triplet σ-pathway surfaces, the reactivity orderings are $L = NCS^- > N_3^- > Cl^- > CF_3CO_2^- > F^- > OH^- > NC^-$, and $L = CF_3CO_2^- > Cl^- > F^- > NCS^- > NC^-$, respectively. Clearly, the oxidant for the σ-pathway behaves in a contrary manner compared with that for the π-pathway, where electron-releasing ligands L diminish the reactivity. It is apparent from Scheme 1, that the strong axial σ-donor ligands (such as NC^- and OH^-) increase the barriers on the quintet surface compared with the weak axial ligands. This result is in accord with a previous suggestion stating that the efficiency of hydrogen abstraction in the quintet state could be attenuated by strong axial σ-donors.[41] These trends may arise from a pushing effect of the σ-donors that destabilizes the σ^*_{z2} orbital, which has strong L–Fe antibonding character and has to be occupied in the σ-pathway on the quintet surface (see Fig. 3).[23,29,36,37,39,40,86] This result is consistent with the experimental observation corresponds to the expected effect of a weaker ligand field from the carboxylate than from the NCMe ligand, leading to reduced destabilization of the σ^*_{z2} orbital.[67] Instead, an opposite trend is obtained for
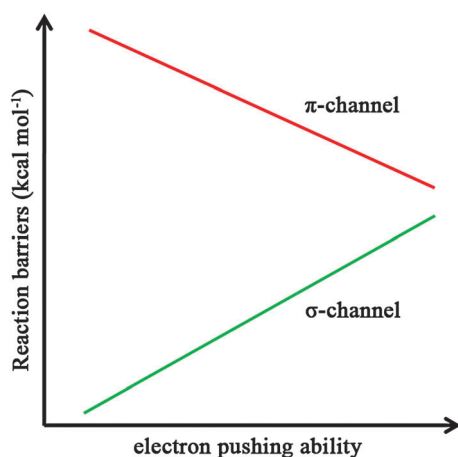
Scheme 1 A schematic representation of the observed trends for the π- and σ-pathways in the methane hydroxylation reaction.

the porphyrin–π-cation radical–Fe(IV)=O reagents,[57,88] where the σ_{z2}^* orbital is populated only past the H-atom abstraction process.[89] Thus, the axial ligand effect is dependent on the system.[86] As a consequence, the axial ligand could affect the reactivity of H-atom abstraction for both the σ- and π-channels, determined by its pushing properties.

4.3 Correlations of the classical reaction channels ($^5\sigma$ and $^3\pi$) barrier height with BDE_{OH}

To ascertain whether or not the trend of H-abstraction reactivity for the distinct reaction channels may be determined by the strength of the formed $(NH_3)_4LFe^{III}(O)$–H bond, we computed the bond dissociation energies (BDEs) of O–H bond in the $(NH_3)_4LFe^{III}(O)$–H species for the classical $^5\sigma$- and $^3\pi$-channels. Table 2 summarizes the barriers of methane hydroxylation by the seven oxidants as well as the BDE_{OH} values of each model and the calculated values of RE_{FeOH} for the transition state structures. Fig. 7 and 8 display the calculated hydrogen abstraction barriers of methane as a function of BDE_{OH}–RE_{FeOH} for the quintet σ- and triplet π-channels, respectively. Inclusion of contribution for RE_{FeOH} gives improvement of the correlation with respect to BDE_{OH} (see Fig. S3 and S4 in ESI†). Excellent linear correlation of $R^2 = 0.9541$ is obtained for the plot of the reaction barriers ($\Delta G^{\ddagger}$) for the triplet π-pathway against BDE_{OH}–RE_{FeOH} in the H-abstraction step. Furthermore, the correlation between the computed quintet σ-pathway barriers ($\Delta G^{\ddagger}$) and the BDE_{OH} values of

Table 2 DFT calculation hydrogen abstraction barriers for $^5\sigma$- and $^3\pi$-pathways by $[Fe^{IV}(O)(NH_3)_4(L)]^+$ (1-L) complexes and the calculated values of BDE_{OH}, RE_{FeOH}

	$BDE_{OH(5\sigma/3\pi)}$	$RE_{FeOH(5\sigma/3\pi)}$	$TS_{H(5\sigma/3\pi)}$[a]
1-F	97.0/90.4	−20.4/−12.7	20.87/26.25
1-NCS	97.5/92.6	−22.3/−15.1	19.89/24.53
1-Cl	96.1/92.0	−21.7/−14.3	20.51/24.85
1-O$_2$CCF$_3$	96.5/92.1	−21.1/−14.5	20.62/24.57
1-N$_3$	96.8/94.8	−21.4/−15.2	20.01/22.97
1-NC	94.7/93.1	−19.7/−15.0	21.68/24.09
1-OH	97.3/94.9	−20.7/−14.0	21.00/23.21

[a] All values are in kcal mol^{-1} and calculated at B3LYP/B2//B3LYP/B1.
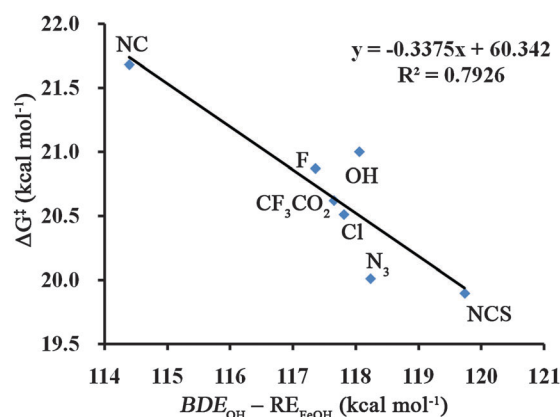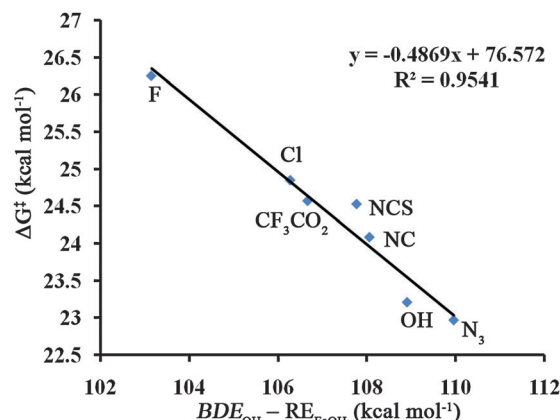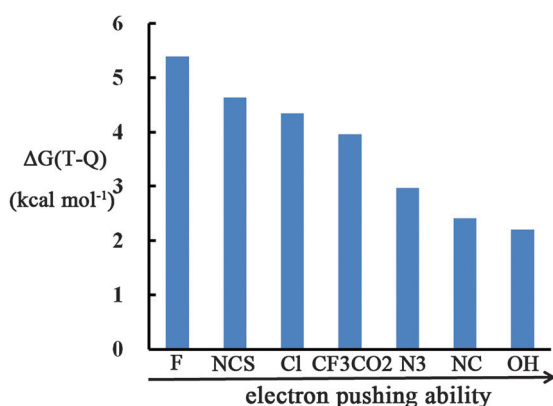

Fig. 7 Correlation of methane hydroxylation $^5\sigma$-pathway barrier height with BDE_{OH} with inclusion of the RE_{FeOH}. Models tested were $[Fe^{IV}(O)(NH_3)_4(L)]^+$ (1-L) with L = N_3^-, OH^-, NC^-, NCS^-, F^-, Cl^-, and $CF_3CO_2^-$.

Fig. 8 Correlation of methane hydroxylation $^3\pi$-pathway barrier height with BDE_{OH} with inclusion of the RE_{FeOH}. Models tested were $[Fe^{IV}(O)(NH_3)_4(L)]^+$ (1-L) with L = N_3^-, OH^-, NC^-, NCS^-, F^-, Cl^-, and $CF_3CO_2^-$.

each model obtained with a correlation coefficient $R^2 = 0.7926$. Therefore, the correlations shown in Fig. 7 and 8 implicate a generally linear correlation between the hydrogen abstraction barrier and BDE_{OH}–RE_{FeOH}. As a result, the calculations described in this work show that the nature of the axial ligand has a greater influence on the BDE_{OH} in the classical $^5\sigma$- and $^3\pi$-channels, similarly to previously reported result that the hydrogen abstraction barriers decrease with the increase of the BDE_{OH} of the oxidants.[90]

4.4 Axial ligand influence on the ΔG(T-Q) gap

The tuning of the energy gap for H-abstraction reaction between the triplet π- and quintet σ-channels by the electron pushing ability of different axial ligands is shown in Scheme 2. An important trend in the $[Fe^{IV}(O)(NH_3)_4L]^+$ series is the decrease in the ΔG(T-Q) gap as the electron pushing effects enhances from L = F^- to L = OH^-. It is clearly seen that the ΔG(T-Q) gap is small when L is a good electron donor (e.g., where L is OH^-) and large when L is a poor electron donor (e.g., where L is F^-).

Scheme 2 A schematic representation of the observed trends for the energy gap between $^3\pi$- and $^5\sigma$-pathways (ΔG(T-Q)) for methane hydroxylation.

Based on this trend we can reason that the ΔG(T-Q) gap is a qualitative expression for the relative energy of the triplet π- and quintet σ-pathways. The reaction channel ordering greatly depends on the interplay between the exchange stabilization which benefits from the ^5TS_H relative to the ^3TS_H in most nonheme enzymes and the destabilization effect of the σ_{z2}^* orbital by the anionic axial ligand.[40,86] Initially, when the degree of the exchange stabilization counteracts the destabilization effect, the quintet σ-pathway will be more effective than the triplet π-pathway. As illustrated in Scheme 2, although the $^5\sigma$ progressively approaches the $^3\pi$ from L = F$^-$, NCS$^-$, Cl$^-$, CF$_3$CO$_2^-$, N$_3^-$, NC$^-$ to OH$^-$, the quintet σ-pathway is energetically favored. In addition, when the exchange stabilization does not exceed, but only offsets the more destabilizating effect of the σ_{z2}^* orbital by the much stronger binding axial σ-donor ligand, the barrier in the quintet σ-pathway will be approximately equal to that in the triplet π-pathway. The calculated small ΔG(T-Q) gap for L = OH$^-$ is not only consist with this hypothesis, but also in agreement with previous studies, which show that the $S = 2$ barrier is remains identical to the triplet barrier in favor of $S = 2$.[86] However, most nonheme enzymes do not have such strong bonding ligands like NC$^-$ and OH$^-$, and hence most enzymes take advantage of the exchange-enhanced reactivity in the quintet σ-pathway.[33,39,40,86]

5. Conclusions

We have performed calculations on extensive [Fe^{IV}(O)(NH$_3$)$_4$L]$^+$ model systems (where L = CF$_3$CO$_2^-$, F$^-$, Cl$^-$, N$_3^-$, NCS$^-$, NC$^-$ and OH$^-$) to study systematically the relative importance of axial ligands in influencing the distinct reaction channels for methane hydroxylation. Density functional theory calculations revealed that all the reactions proceed via more than one channel. In contrast to the nonclassical pathways ($^3\sigma$, $^5\pi$), the classical channels ($^3\pi$, $^5\sigma$) can bring more satisfactory performance, as we expected. According to our results, it is clear that the electron pushing ability of the axial ligand can exert a considerable influence on the distinct reaction channel reactivities. Interestingly, the σ-pathway reactivity decreases as the electron-donating ability of the axial ligand strengthens, while the π-pathway reactivity follows an opposite trend. From the qualitative perspective, both trends lead to the observation that the barrier gap between the $^3\pi$

and $^5\sigma$ (ΔG(T-Q)) decreases as the electron pushing ability of the axial ligand increases. Moreover, the apparently antielectrophilic trend observed for ΔG(T-Q) stems from the fact that the triplet π- and quintet σ-channels can be fine-controlled by the interplay between the exchange-stabilization benefiting from the ^5TS_H relative to the ^3TS_H in most nonheme enzymes and the destabilization effect of the σ_{z2}^* orbital by the anionic axial ligand. When the former counteracts the latter, the quintet σ-pathway will be more effective than the other alternatives. However, when the dramatic destabilization effect of the σ_{z2}^* orbital by a strong binding axial σ-donor ligand like OH$^-$ only counteracts, but does not override the exchange-stabilization, the barrier in the quintet σ-pathway will remain identical to the triplet π-pathway barrier. Indeed, the axial ligands do not change the intrinsic reaction mechanism in their respective pathways; however, they can affect the energy barriers of different reaction channels for C–H activation. Therefore, we may provide a simple and effective approach for tuning the quintet σ-channel reactivity by increasing/decreasing the electron pushing ability.

Besides steric hindrance in model systems, or the restrictions of the protein pocket in metalloenzymes,[23] tuning the electron-donating character of the axial ligand can also alter the reactivity of the different reaction channels. The insight gained in this work may provide theoretical guidance for experimentally devising catalytic species with superior reactivity of the Fe^{IV}=O moiety.

Acknowledgements

Notes and references

1 E. I. Solomon, T. C. Brunold, M. I. Davis, J. N. Kemsley, S. K. Lee, N. Lehnert, F. Neese, A. J. Skulan, Y. S. Yang and J. Zhou, *Chem. Rev.*, 2000, **100**, 235–349.
2 I. Schlichting, J. Berendzen, K. Chu, A. M. Stock, S. A. Maves, D. E. Benson, R. M. Sweet, D. Ringe, G. A. Petsko and S. G. Sligar, *Science*, 2000, **287**, 1615–1622.
3 T. Spolitak, J. H. Dawson and D. P. Ballou, *J. Biol. Chem.*, 2005, **280**, 20300–20309.
4 S. Shaik, D. Kumar, S. P. de Visser, A. Altun and W. Thiel, *Chem. Rev.*, 2005, **105**, 2279–2328.
5 A. Altun, S. Shaik and W. Thiel, *J. Am. Chem. Soc.*, 2007, **129**, 8978–8987.
6 J. C. Schöneboom, F. Neese and W. Thiel, *J. Am. Chem. Soc.*, 2005, **127**, 5840–5853.
7 P. G. Debrunner, A. F. Dexter, C. E. Schulz, Y. M. Xia and L. P. Hager, *Proc. Natl. Acad. Sci. U. S. A.*, 1996, **93**, 12791–12798.
8 R. Rutter, M. Valentine, M. P. Hendrich, L. P. Hager and P. G. Debrunner, *Biochemistry*, 1983, **22**, 4769–4774.
9 R. Rutter, L. P. Hager, H. Dhonau, M. Hendrich, M. Valentine and P. Debrunner, *Biochemistry*, 1984, **23**, 6809–6816.
10 C. E. Schulz, R. Rutter, J. T. Sage, P. G. Debrunner and L. P. Hager, *Biochemistry*, 1984, **23**, 4743–4754.
11 S. P. de Visser, S. Shaik, P. K. Sharma, D. Kumar and W. Thiel, *J. Am. Chem. Soc.*, 2003, **125**, 15779–15788.
12 J. C. Price, E. W. Barr, B. Tirupati, J. M. Bollinger Jr. and C. Krebs, *Biochemistry*, 2003, **42**, 7497–7508.
13 J. C. Price, E. W. Barr, T. E. Glass, C. Krebs and J. M. Bollinger Jr., *J. Am. Chem. Soc.*, 2003, **125**, 13008–13009.

14 P. J. Riggs-Gelasco, J. C. Price, R. G. Guyer, J. H. Brehm, E. W. Barr, J. M. Bollinger Jr. and C. Krebs, *J. Am. Chem. Soc.*, 2004, **126**, 8108–8109.

15 D. A. Proshlyakov, T. F. Henshaw, G. R. Monterosso, M. J. Ryle and R. P. Hausinger, *J. Am. Chem. Soc.*, 2004, **126**, 1022–1023.

16 K. Yoshizawa, T. Yumura, Y. Shiota and T. Yamabe, *Bull. Chem. Soc. Jpn.*, 2000, **73**, 29–36.

17 G. Yang, D. Zhou, X. Liu, X. Han and X. Bao, *J. Mol. Struct.*, 2006, **797**, 131–139.

18 W. Nam, *Acc. Chem. Res.*, 2007, **40**, 522–531.

19 C. Krebs, D. G. Fujimori, C. T. Walsh and J. M. Bollinger Jr., *Acc. Chem. Res.*, 2007, **40**, 484–492.

20 O. Pestovsky, E. Münck, S. Stoian, E. L. Bominaar, X. P. Shan, L. Que Jr. and A. Bakac, *Angew. Chem., Int. Ed.*, 2005, **44**, 6871–6874.

21 J. England, Y. Guo, E. R. Farquhar, V. G. Young Jr., E. Muenck and L. Que Jr., *J. Am. Chem. Soc.*, 2010, **132**, 8635–8644.

22 D. C. Lacy, R. Gupta, K. L. Stone, J. Greaves, J. W. Ziller, M. P. Hendrich and A. S. Borovik, *J. Am. Chem. Soc.*, 2010, **132**, 12188–12190.

23 A. Decker, J. Rohde, E. J. Klinker, S. D. Wong, L. Que Jr. and E. I. Solomon, *J. Am. Chem. Soc.*, 2007, **129**, 15983–15996.

24 J. C. Schöneboom, S. Cohen, H. Lin, S. Shaik and W. Thiel, *J. Am. Chem. Soc.*, 2004, **126**, 4017–4034.

25 D. Kumar, H. Hirao, L. Que Jr. and S. Shaik, *J. Am. Chem. Soc.*, 2005, **127**, 8026–8027.

26 S. Shaik, D. Kumar and S. P. de Visser, *J. Am. Chem. Soc.*, 2008, **130**, 10128–10140.

27 P. E. M. Siegbahn and T. Borowski, *Acc. Chem. Res.*, 2006, **39**, 729–738.

28 B. Ensing, F. Buda, M. C. M. Gribnau and E. J. Baerends, *J. Am. Chem. Soc.*, 2004, **126**, 4355–4365.

29 C. Michel and E. J. Baerends, *Inorg. Chem.*, 2009, **48**, 3628–3638.

30 S. P. de Visser, *J. Am. Chem. Soc.*, 2006, **128**, 9813–9824.

31 S. P. de Visser, *J. Am. Chem. Soc.*, 2006, **128**, 15809–15818.

32 C. Y. Geng, S. F. Ye and F. Neese, *Angew. Chem., Int. Ed.*, 2010, **49**, 5717–5720.

33 S. F. Ye and F. Neese, *Proc. Natl. Acad. Sci. U. S. A.*, 2011, **108**, 1228–1233.

34 S. F. Ye and F. Neese, *Curr. Opin. Chem. Biol.*, 2009, **13**, 89–98.

35 S. Shaik, M. Filatov, D. Schröder and H. Schwarz, *Chem.–Eur. J.*, 1998, **4**, 193–199.

36 H. Hirao, D. Kumar, L. Que Jr. and S. Shaik, *J. Am. Chem. Soc.*, 2006, **128**, 8590–8606.

37 H. Hirao, L. Que Jr., W. Nam and S. Shaik, *Chem.–Eur. J.*, 2008, **14**, 1740–1756.

38 H. Hirao, D. Kumar, W. Thiel and S. Shaik, *J. Am. Chem. Soc.*, 2005, **127**, 13007–13018.

39 D. Janardanan, Y. Wang, P. Schyman, L. Que Jr. and S. Shaik, *Angew. Chem., Int. Ed.*, 2010, **49**, 3342–3345.

40 S. Shaik, H. Chen and D. Janardanan, *Nat. Chem.*, 2010, **3**, 19–27.

41 L. Bernasconi, M. L. Louwerse and E. J. Baerends, *Eur. J. Inorg. Chem.*, 2007, 3023–3033.

42 M. J. Louwerse and E. J. Baerends, *Phys. Chem. Chem. Phys.*, 2007, **9**, 156–166.

43 E. I. Solomon, S. D. Wong, L. V. Liu, A. Decker and M. S. Chow, *Curr. Opin. Chem. Biol.*, 2009, **13**, 99–113.

44 J. Rossmeisl, K. Dimitrievski, P. Siegbahn and J. K. Nørskov, *J. Phys. Chem. C*, 2007, **111**, 18821–18823.

45 J. H. Dawson, R. H. Holm, J. R. Trudell, G. Barth, R. E. Linder, E. Bunnenberg, C. Djerassi and S. C. Tang, *J. Am. Chem. Soc.*, 1976, **98**, 3707–3709.

46 J. H. Dawson and M. Sono, *Chem. Rev.*, 1987, **87**, 1255–1276.

47 J. H. Dawson, *Science*, 1988, **240**, 433–439.

48 M. Sono, M. P. Roach, E. D. Coulter and J. H. Dawson, *Chem. Rev.*, 1996, **96**, 2841–2887.

49 Z. Gross and S. Nimri, *Inorg. Chem.*, 1994, **33**, 1731–1732.

50 Z. Gross, *JBIC, J. Biol. Inorg. Chem.*, 1996, **1**, 368–371.

51 K. Czarnecki, S. Nimri, Z. Gross, L. M. Proniewicz and J. R. Kincaid, *J. Am. Chem. Soc.*, 1996, **118**, 2929–2935.

52 C. V. Sastri, M. J. Park, T. Ohta, T. A. Jackson, A. Stubna, M. S. Seo, J. Lee, J. Kim, T. Kitagawa, E. Münck, L. Que Jr. and W. Nam, *J. Am. Chem. Soc.*, 2005, **127**, 12494–12495.

53 W. J. Song, Y. O. Ryu, R. Song and W. Nam, *JBIC, J. Biol. Inorg. Chem.*, 2005, **10**, 294–304.

54 C. V. Sastri, J. Lee, K. Oh, Y. J. Lee, J. Lee, T. A. Jackson, K. Ray, H. Hirao, W. Shin, J. A. Halfen, J. Kim, L. Que Jr., S. Shaik and W. Nam, *Proc. Natl. Acad. Sci. U. S. A.*, 2007, **104**, 19181–19186.

55 T. A. Jackson, J.-U. Rohde, M. S. Seo, C. V. Sastri, R. DeHont, A. Stubna, T. Ohta, T. Kitagawa, E. Münck, W. Nam and L. Que Jr., *J. Am. Chem. Soc.*, 2008, **130**, 12394–12407.

56 S. Fukuzumi, H. Kotani, T. Suenobu, S. Hong, Y.-M. Lee and W. Nam, *Chem.–Eur. J.*, 2009, **15**, 354–361.

57 Y. Kang, H. Chen, Y. J. Jeong, W. Lai, E. H. Bae, S. Shaik and W. Nam, *Chem.–Eur. J.*, 2009, **15**, 10039–10046.

58 S. P. de Visser, R. Latifi, L. Tahsini and W. Nam, *Chem.–Asian J.*, 2011, **6**, 493–504.

59 T. Kamachi, T. Kouno, W. Nam and K. Yoshizawa, *J. Inorg. Biochem.*, 2006, **100**, 751–754.

60 D. Kumar, G. N. Sastry and S. P. de Visser, *J. Phys. Chem. B*, 2012, **116**, 718–730.

61 J.-U. Rohde, J.-H. In, M. H. Lim, W. W. Brennessel, M. R. Bukowski, A. Stubna, E. Münck, W. Nam and L. Que Jr., *Science*, 2003, **299**, 1037–1039.

62 M. Costas, M. P. Mehn, M. P. Jensen and L. Que Jr., *Chem. Rev.*, 2004, **104**, 939–986.

63 W. Balland, M. F. Charlot, F. Banse, J. J. Girerd, T. A. Mattioli, E. Bill, J. F. Bartoli, P. Battioni and D. Mansuy, *Eur. J. Inorg. Chem.*, 2004, 301–308.

64 J. F. Berry, E. Bill, E. Bothe, T. Weyhermüller and K. Wieghardt, *J. Am. Chem. Soc.*, 2005, **127**, 11550–11551.

65 M. P. Jensen, M. Costas, R. Y. N. Ho, J. Kaizer, A. Mairata i Payeras, E. Münck, L. Que Jr., J.-U. Rohde and A. Stubna, *J. Am. Chem. Soc.*, 2005, **127**, 10512–10525.

66 J. Kaizer, E. J. Klinker, N. Y. Oh, J.-U. Rohde, W. J. Song, A. Stubna, J. Kim, E. Münck, W. Nam and L. Que Jr., *J. Am. Chem. Soc.*, 2004, **126**, 472–473.

67 J.-U. Rohde and L. Que Jr., *Angew. Chem., Int. Ed.*, 2005, **44**, 2255–2258.

68 F. Neese, *ORCA – an ab initio, Density Functional and Semiempirical Program Package Version 2.8 ed.*, University of Bonn, Bonn (Germany), 2010.

69 F. Weigend and R. Ahlrichs, *Phys. Chem. Chem. Phys.*, 2005, **7**, 3297–3305.

70 A. D. Becke, *J. Chem. Phys.*, 1993, **98**, 5648–5652.

71 C. T. Lee, W. T. Yang and R. G. Parr, *Phys. Rev. B*, 1988, **37**, 785–789.

72 A. Schäfer, C. Huber and R. Ahlrichs, *J. Chem. Phys.*, 1994, **100**, 5829–5835.

73 F. Neese, F. Wennmohs, A. Hansen and U. Becker, *Chem. Phys.*, 2009, **356**, 98–109.

74 K. Eichkorn, O. Treutler, H. Ohm, M. Häser and R. Ahlrichs, *Chem. Phys. Lett.*, 1995, **240**, 283–290.

75 K. Eichkorn, F. Weigend, O. Treutler and R. Ahlrichs, *Theor. Chem. Acc.*, 1997, **97**, 119–124.

76 K. Eichkorn, O. Treutler, H. Ohm, M. Häser and R. Ahlrichs, *Chem. Phys. Lett.*, 1995, **242**, 652–660.

77 F. Weigend, M. Häser, H. Patzelt and R. Ahlrichs, *Chem. Phys. Lett.*, 1998, **294**, 143–152.

78 F. Weigend, A. Kohn and C. Hattig, *J. Chem. Phys.*, 2002, **116**, 3175–3183.

79 S. Grimme, *J. Comput. Chem.*, 2006, **27**, 1787–1799.

80 P. E. M. Siegbahn, M. R. A. Blomberg and S.-L. Chen, *J. Chem. Theory Comput.*, 2010, **6**, 2040–2044.

81 C. Adamo and V. Barone, *J. Chem. Phys.*, 1999, **110**, 6158–6170.

82 A. Fouqueau, M. E. Casida, L. M. Lawson Daku, A. Houser and F. Neese, *J. Chem. Phys.*, 2005, **122**, 044110.

83 F. Neese, *J. Inorg. Biochem.*, 2006, **100**, 716–726.

84 J. T. Groves and G. A. McClusky, *J. Am. Chem. Soc.*, 1976, **98**, 859–861.

85 R. Lonsdale, J. N. Harvey and A. J. Mulholland, *J. Phys. Chem. Lett.*, 2010, **1**, 3232–3237.

86 H. Chen, W. Z. Lai and S. Shaik, *J. Phys. Chem. Lett.*, 2010, **1**, 1533–1540.

87 D. Janardanan, D. Usharani, H. Chen and S. Shaik, *J. Phys. Chem. Lett.*, 2011, **2**, 2610–2617.

88 A. Takahashi, T. Kurahashi and H. Fujii, *Inorg. Chem.*, 2009, **48**, 2614–2625.

89 S. Shaik, S. Cohen, Y. Wang, H. Chen, D. Kumar and W. Thiel, *Chem. Rev.*, 2010, **110**, 949–1017.

90 S. P. de Visser, *J. Am. Chem. Soc.*, 2010, **132**, 1087–1097.